Supplementary Materials for

In vivo Architecture and Action of Bacterial Structural Maintenance of Chromosome Proteins

Anjana Badrinarayanan, Rodrigo Reyes-Lamothe, Stephan Uphoff,
Mark C. Leake,* David J. Sherratt*

*To whom correspondence should be addressed.
E-mail: m.leake1@physics.ox.ac.uk (M.C.L.); david.sherratt@bioch.ox.ac.uk (D.J.S.)

Published 26 October 2012, *Science* **338**, 528 (2012)
DOI: 10.1126/science.1227126

This PDF file includes:

Materials and Methods

Construction of fluorescent fusions of MukBEF

All strains were derivatives of *E. coli* K12 AB1157 (*27*) and new strains were constructed using λ-Red recombination (*9, 28*). Oligonucleotides had a 50 nucleotide complementary sequence to the last 50 base pairs of the gene (not including the stop codon) or 50 base pairs downstream, followed by 20 nucleotides complementary to an 11 aa linker or the end of the kanamycin/chloramphenicol resistance cassette in the plasmid, respectively. Polymerase chain reaction (PCR) used plasmids described previously (*29*) as templates (these plasmids code for an 11 aa linker followed by YPet, mCherry or PAmCherry and an antibiotic resistance cassette). The DNA fragment was gel purified and 1μg was electrotransformed into AB1157 derivative cells over-expressing λ-Red proteins from pKD46. Cells were selected on plates with appropriate antibiotic and insertion into the chromosome was checked by PCR. MukB and MukE fluorescent fusions were constructed in the chromosome at the original location of the genes by λ-Red recombination. Primers used to construct *mukB-YPet* were: Forward 5'- AAC TCC CTG AAA CGC TTC CAG GAA CTG ACG AAG CGC CTT CTC AGG CGA GTT CGG CTG GCT CCG CTG C -3' Reverse: 5'- GA AAC GGA GTT TTC GGA AAA AGA AAA GGC GGC ATT GCT GCC GCC TTA ATT CTT ATG AAT ATC CTC CTT AGT TC- 3'

mukE-YPet Forward: 5’ - AAC TCA ACG ATG AAA CCG AAG AGA ATC AGC CAG ATA GCG GAG AGG AAG AAT CGG CTG GCT CCG CTG C -3’ Reverse: GTT CCA GTT AAT CAG CGT CAG TGA GCG AAA TTT ACC GCG TTC AAT CAT TAC TTA TGA ATA TCC TCC TTA GTT C- 3’.

For *mukF*, N-terminal fusions (antibiotic resistance cassette flanked by *frt* sites, followed by *YPet*, *mCherry* or *PAmCherry*) was constructed using the following primers: 5’- GTT ATA TTC ATG TCA CCG CGC GCA AAC CGC AGA GCA AGG ATA AAG TAT GA T GTA GGC TGG AGC TGC TTC G – 3’ Reverse: 5’ – TTT CTG GCC CAG GCA ACC AGT TCG GGG ACT GTC TGG GAA AAT TCA CTC AT CGC GCT GCC AGA ACC AGC – 3’

For two color experiments, first λ-Red fusions of *mukF* or *mukE-mCherry* were constructed and the antibiotic resistance cassette was then removed using Flp recombinase. Following this, GFP (with Cm antibiotic resistance cassette) was integrated at the C-terminus of MukB using λ-Red recombination.

Function of fluorescent fusions was tested by assessing growth in minimal and rich media. Growth rates were similar to wild type in minimal media with glycerol as the carbon source and in rich media. No abnormal cell filamentation or production of anucleate cells was observed. Furthermore, position of the origin region (as assessed using the fluorescent operator-repressor system) was as wild type in strains carrying fluorescent fusions of MukBEF. Additionally, the fluorescent spots localized to the origin region as seen previously (*6*).

Construction of $MukB_{EQ}$-GFP and $MukB_{DA}$-GFP

Using the primers (Forward 5'- AAC GTA TCG TTT GGT CAG G-3'; Reverse 5'- TT GAG ATT CGA TTT GCG TGC-3') the 3' end of *mukB* fused to *GFP* followed by a *Cm* resistance cassette (1175 bp without GFP and antibiotic cassette) was amplified and cloned into a pGemT vector (Promega cat. no A1360). Site-directed mutagenesis was carried out on the resultant plasmid to introduce the D1406A mutation using the primer set: Forward 5'- T GCT GTT CCT CGC TGA AGC AGC GCG –3'; Reverse 5'- CGC GCT GCT TCA GCG AGG AAC AGC A –3'. For the E1407Q mutation the primer set was: Forward 5'- CTG CTG TTC CTC GAT CAG GCA GCG CGA CTG GAT -3'; Reverse 5'- ATC CAG TCG CGC TGC CTG ATC GAG GAA CAG CAG -3' Insertion of the mutation was checked by sequencing. The fragment was then reintroduced into the chromosome (at the endogenous locus) by λ-Red recombination using the following primers: Forward 5'- AAC GTA TCG TTT GGT CAG G-3'; Reverse 5'- TT GAG ATT CGA TTT GCG TGC-3'. Insertion was checked by assaying temperature sensitivity (cells could grow in LB at 22°C and not 37°C) and by sequencing/ PCR. Microscopically, the mutants had filamentous growth in rich media and increased production of anucleate cells in rich and minimal media (as reported for Muk^- cells).

Construction of $MukB_{EQ}$, $MukB_{DA}$ and $MukB_{SR}$ variants

Using the primers (Forward 5'- AAC GTA TCG TTT GGT CAG G-3'; Reverse 5'- TT GAG ATT CGA TTT GCG TGC-3') the 3' end of *mukB* fused to *mYPet* followed by a *Km* resistance cassette or only with an antibiotic cassette (1175 bp without the fusion and antibiotic cassette) were amplified and cloned into a pGemT vector (Promega cat. no

A1360). Site-directed mutagenesis was carried out on the resultant plasmid to introduce the D1406A mutation using the primer set: Forward 5'- T GCT GTT CCT CGC TGA AGC AGC GCG –3'; Reverse 5'- CGC GCT GCT TCA GCG AGG AAC AGC A –3'. The E1407Q mutation was introduced into MukB using the primer set: Forward 5'- CTG CTG TTC CTC GAT CAG GCA GCG CGA CTG GAT -3'; Reverse 5'- ATC CAG TCG CGC TGC CTG ATC GAG GAA CAG CAG -3' and the S1366R mutation was introduced using the primer set: Forward 5' - GAG TCT GGT GCA TTG CGG ACC GGT GAG GCG ATT; Reverse 5' - AAT CGC CTC ACC GGT CCG CAA TGC ACC AGA CTC.

Insertion of the mutation was checked by sequencing. The fragment was then reintroduced into the chromosome (at the endogenous locus) by λ-Red recombination using the following primers: Forward 5'- AAC GTA TCG TTT GGT CAG G-3'; Reverse 5'- TT GAG ATT CGA TTT GCG TGC-3'. For mutant strains carrying MukE- or MukF-mYPet fusions, first λ-Red fusions of *mukF* or *mukE-mYPet* were constructed. The antibiotic resistance cassette was removed using Flp recombinase. Following this, the fragment containing the 3' end of *mukB* with the mutation and antibiotic cassette only were reintroduced into the chromosome (at the endogenous locus) by the process of λ-Red recombination using the primers described above. Insertion was checked by assaying temperature sensitivity (cells could grow in LB at 22°C and not 37°C) and by sequencing/ PCR. Microscopically, the mutants had filamentous growth in rich media and increased production of anucleate cells in rich and minimal media (as reported for Muk^- cells).

Western blotting of Muk fusions

Cells were grown in LB to an OD_{600} of ~0.5, centrifuged at 4 krpm for 10min at 4^{o}C, resuspended in 90 ml of Cracking Buffer (50 mM Tris-HCl, pH 6.8, 100 mM dithiothreitol, 2% SDS, 0.1% bromphenol blue, and 10% glycerol). Samples were boiled for 10 minutes at 97°C before loading into an SDS-PAGE gel with a 5% or 10% acrylamide separation gel (for MukB or MukE/MukF, respectively). Transfer was performed using the Invitrogen iBlot system. Membrane was blocked with 5% milk (in PBS) overnight at 4^{o}C. The blot was probed with primary antibody (1:3000 to 1:5000 dilution in 0.5% milk+PBST or 5 ml Signal Boost solutionI (Thermoscientific cat no. 46640), and then with secondary antibody (1:5000 dilution in 0.5% milk+PBST or 5ml Signal Boost solutionII). A list of primary and secondary antibodies used is described in table S1. Immunoreactive bands were visualized on blots by using an enhanced chemiluminescence kit (ECL, Thermoscientific cat no. 32109)**.**

Preparation of cells for microscopy

Cells were grown in LB until stationary phase and subcultured overnight in M9-glycerol. The following day, cells were subcultured in fresh media and grown till OD 0.05-0.15 before imaging. Cells were concentrated and laid on an M9-glycerol 1% agarose pad. In order to elongate cells for FRAP experiments, cells were allowed to grow for ~2 h in the presence of the cell division inhibitor, cephalexin (100 mg/ml). Cells were then concentrated and laid on an M9-glycerol 1% agarose pad containing cephalexin.

Estimation of immature fraction of YPet, mCherry and GFP

The proportion of any putative dark, immature fraction of YPet, mCherry or GFP was estimated by photobleaching cells carrying derivatives of MukB GFP, YPet or mCherry completely in the presence of 50 μg/ml of chloramphenicol to prevent further protein expression. Total cellular fluorescence intensity was measured every 15 min for up to 90 min after complete cellular bleaching, to assess the extent of any recovery which would be indicative of maturation of a previously immature fraction. This indicated a mean measurable recovery of fluorescence intensity of less than 5% over this time scale.

We then performed analysis based on this measured maximum value of fluorescence recovery and the measured cell doubling time of our strains at room temperature to estimate the likely proportion of any 'dark' (i.e. immature) fluorescent protein in a cell at the typical time of fluorescence slimfield imaging following cell cultivation and microscope sample preparation. The recovery fluorescence intensity $I(t)$ at a time t in min after a full cellular photobleach can be modeled as a simple exponential process, since the 'depletion' of the dark population (i.e. the maturation process) is a first-order reaction:

$$I(t) = I(\infty)\left(1 - \exp\left[-\left(\Delta t + t\right)/t_m\right]\right)$$

Here, $I(\infty)$ is the fully recovered intensity of any previously dark protein, t_m is the exponential 'maturation time' and Δt is the characteristic time between fluorescent protein being first expressed in a given cell under observation and the start of the photobleach (in other words, it is a 'head start' time for the maturation of any dark protein). Although individual cells in a population may be at different stages in their cell cycles, the 'average' cell, assuming we sample many cells over time from that

population, will be roughly mid-cycle. If the cell doubling time is t_d then on average $\Delta t=t_d/2$. Although for cells grown in M9-glycerol at 37°C have t_d values of ~100 min (see Supplementary Methods, table S3) the equivalent values under our imaging conditions of room temperature are more like ~4 h, or ~240 min. Thus, since the increase in measured fluorescence 90 min following the photobleach is less than 5% we can say:

$$\frac{I(90)}{I(0)} = \frac{(1-\exp[-(240/2+90)/t_m])}{(1-\exp[-(0+90)/t_m])} = \frac{(1-\exp[-210/t_m])}{(1-\exp[-90/t_m])} \leq 1.05$$

Solving this equation numerically indicates a maximum value of ~41 min for t_m, which is close to the measured maturation time for Clontech enhanced GFP reported elsewhere (*10*). The typical time delay between cultivating cells from their LB growth medium, preparing the microscope sample slide and then actually imaging the cells during typical slimfield experiments is roughly 1 h, or ~60 min. This indicates that the likely maximum proportion of dark protein present in such cells will be ~exp[-(240/2+60)/41], or ~1%. This indicates that for a MukBEF complex to have in excess of one dark fluorescent protein molecule present then its typical stoichiometry in terms of total number of fluorescent protein molecules per complex would need to be in excess of ~100 molecules, which is ~3 times greater than the average stoichiometry we observe of MukB and MukE immobile spots, and over 5 times greater than the average MukF stoichiometry of immobile spots.

Single color slimfield imaging and fluorescent spot analysis

A single color home-built laser excitation slimfield microscope was used for YPet cell strain imaging capable of single molecule detection over a millisecond time scale, similar to that reported previously (*9*). In brief, this involved a bespoke inverted fluorescence microscope with a 100x Plan Fluor 1.49 NA oil immersion objective (Nikon) and an *xyz* nanometre-precise positioning stage (Mad City Labs). Brightfield illumination used a tungsten-halogen source; laser excitation used a TEM00 plane-polarized continuous-wave 532 nm DPSS laser (Laser2000 UK) and filtered (laser-line 532 nm) and circularized using a $\lambda/4$ plate. The separately-shuttered slimfield excitation laser beam width was shrunk by a factor of three using a Galilean de-expander and the collimated laser beam directed to under-fill the back-aperture of the objective lens. This generated a conflated confocal volume profile at the sample whose measured Gaussian standard deviation width in the focal plane was ~3 μm (FWHM of ~7 μm) with intensity ~6.5 kW cm^{-2}, allowing quantitative detection of single fluorescent molecules at 3 ms capture rates in single *E. coli* cells which permitted visualization of fast diffusing proteins which appear blurred and hidden by camera noise using slower video-rate microscopy.

Fluorescence emissions were passed through a dichroic mirror, filtered using a band-pass emission filter and imaged at ~40 nm per pixel in frame-transfer mode by a 128x128-pixel, cooled, back-thinned electron-multiplying charge-coupled-device camera (iXon+ DV860-BI, Andor Technology, UK). A maximum of 100 continuously illuminated frames were taken in each run.

Images were analyzed using a custom-written toolkit in LabVIEW 8.5 reported previously (*9*). In brief, the perimeters of cell bodies were identified using custom-written recognition software from the brightfield images, used to create an image mask for subsequent fluorescence analysis. Then, a frame-average image was complied from typically a 90 ms total integration time. 'Hotspots' in intensity of the frame-averaged image indicating localized fluorescent spots could then clearly be observed and a preliminary intensity centroid position assigned. A circular region of interest (ROI) was created around each putative spot of diameter 16 pixels, large enough to encapsulate each hotspot including those showing elongation parallel to the long-axis of the cell. Having defined the position of the ROI on the frame-averaged image, analysis was then performed on the raw data series, one image at a time, letting the outer ROI position remain fixed but allowing an inner circular ROI within this to vary its position to best fit the intensity centroid. The intensity in each ROI was modeled as a radial Gaussian plus a uniform baseline of background noise. The intensity contribution due to the YPet (the 'spot intensity') was calculated thus:

1. An inner circular mask was created for the contribution of the spot of diameter 5 pixels to the ROI centered on the intensity centroid.

2. We convolved intensities within this mask by a 2D radial Gaussian function of fixed width 3 pixels and generated a new estimate for the centroid.

3. We iterated steps 1-2 until convergence (less than 10 loops). For an integration time of 3 ms per image using surface-immobilized YPet as the sample this resulted in an ultimate centroid r.m.s. precision of ~50 nm.

4. We defined the background intensity as the median intensity within the fixed ROI external to the inner circle mask. The contribution to the background count due to diffusive YPet in the cytoplasm (i.e. that not bound in a localized MukBEF complex) was calculated for each track as the initial background intensity per pixel after subtracting the autofluorescence contribution per pixel measured in the non-YPet parental strain and the instrumental background.

5. A preliminary spot intensity $I(t)$ at a time t was defined as the sum of all intensities within the inner circular mask after subtraction of the background from each individual pixel value.

6. A small correction to the spot intensity was applied to account for non-uniformity in the slimfield confocal volume due to its Gaussian shape in the sample plane: we multiplied each spot intensity by the factor $\exp(r^2/2\sigma_{xy}^2)$ where r is the distance from the spot centroid to the center of the slimfield excitation volume in the sample plane and σ_{xy} is the standard deviation width of the excitation field (3 μm). Even for the longest bacterial cells in which the spots were most distant from the center of the slimfield volume the correction factor never exceeded 1.1 (i.e. less than 10% difference between corrected and pre-corrected values).

7. A Gaussian fit was then performed on the spot intensity component optimizing both amplitude and width, generating an estimate for the size of the spot.

This resulted in an automated method for characterizing fluorescent MukBEF spots on each separate image frame within the fixed hotspot ROI which could quantify the total

pixel intensity minus the background detector noise, the size of the spots and the position of the spot to within typically ~50 nm precision.

Spot intensity data were collated for each cell strain and the distribution of estimated pixel intensity binned on a histogram. This resulted in multiple distinct peaks separated by a roughly constant spacing, with the center of the lowest order peak within typically ~10% of the unitary photobleaching peak measured for surface immobilized pure YPet performed *in vitro* (Fig. 1). We also performed experiments on purified YPet by immobilizing the protein to the coverslip surface using conjugation via the anti-YPet antibody (*9*), which as found previously was also in reasonable agreement with estimating the unitary peak with a Fourier spectral method which constructed a power spectrum from the periodicity in the intensity trace, made up of an edge-preserving Chung-Kennedy algorithm of two adjacent windows run across the data whose output was the mean from the window possessing the smallest variance.

The most reliable method for these data, as had been found from our earlier slimfield study of the bacterial replisome (*9*), was estimation of the size of the unitary YPet photobleaching step in intensity by performing a multiple Gaussian fit to the collated, binned spot intensity data, and taking the center of the lower order peak as the best estimate for the unitary step size of YPet in vivo in that particular cell strain, I_{YPet}, indicating ~1,100 counts (fig. S7B) on our detector across the different cell strains used in this study, with a ~20% variation between datasets. The raw intensity trace as a function of time t for each individual fluorescent spot was fitted by a single exponential decay function $I(t)=I_0\exp(-t/t_b)$, where t_b is the optimized photobleach time, estimated to

be in the range 30-50 ms consistent with earlier findings (*9*). The number of YPet molecules associated with each fluorescent spot was then estimated as I_0 divided by I_{YPet}.

For each cell strain we constructed the stoichiometry distribution using an unbiased kernel density estimation (KDE) via a Parzen window method which convolved the stoichiometry dataset with a Gaussian kernel of set width s equal to the noise of the measurement (equivalent to typically 0.7-1.0 YPet molecules in terms of peak-to-peak amplitude of the intensity signal), normalized the area of each Gaussian to be unity to represent a single data point measurement. The periodicity of each KDE was then evaluated by first calculating the pair-wise difference distribution in the KDE, in a similar method used for the Fourier spectral analysis, and then generating the power spectrum of this difference distribution as the square of the Fast Fourier Transform (FFT), taking the reciprocal of the spatial frequency axis to convert this into intensity counts and using a Nyquist lower limit cut-off equivalent to 2s.

Live-cell PALM imaging and analysis

To obtain higher resolution data on the immobile and diffusing spots, we used PALM super-resolution microscopy (*11*, *32*) on photo-activatable mCherry, PAmCherry (*33*), in functional fusion strains of *E. coli* to all three of the MukBEF components in live cells (Supplementary Methods). We developed an imaging modality to identify individual bound and diffusing molecules (SU, RR-L, Garza de Leon, F., DJS. & Kapanidis, A., unpublished), applied here to resolve the spatial distribution of molecules within immobile MukBEF clusters and measure the diffusion of unbound complexes. Briefly, imaging was performed on a custom-built widefield fluorescence microscope with a 561 nm laser (SLIM-561 200 mW, Oxxius, France) and photo-activated with a 405 nm laser (MLL-III-405 100 mW, CNI, China). The 561 nm and 405 nm laser beams were directed (100x oil immersion objective, NA 1.4, Olympus, Japan) onto the sample under an angle allowing for near total internal reflection. Fluorescence emission was filtered (ZT405/473/561rpc and ZET405/473/561NF, Chroma, USA) and imaged on an EMCCD camera (iXon, Andor, UK) at magnification 114 nm/pixel. Cell outlines were recorded with an LED brightfield light source (pE-100, coolLED, UK) via an Olympus condenser (IX-2, Olympus, Japan) on the same microscope. Sample position and focus were controlled with a motorized stage and *z*-motor (ASIimaging, USA).

Brightfield images of the cell outlines were recorded before super-resolution imaging (fig. S4). PALM movies for protein tracking were recorded under continuous 561 nm wavelength excitation at power 3.5 mW at 50 ms/frame for ~5000 frames. The density of active PAmCherry was controlled by adjusting 405 nm excitation from

~0-15 μW. We tracked individual photo-activated molecules over multiple consecutive localizations (*34, 35*). Super-resolution localization analysis was performed using custom-written MATLAB software (Mathworks, USA). Single molecule point spread function intensity profiles were identified for localization by band-pass filtering and applying a fixed intensity threshold to each frame of a super-resolution movie. Candidate positions were used as initial guesses to fit an unconstrained two-dimensional elliptical Gaussian function for super-resolution localization (*36, 37*). Single particle tracking analysis was performed by adapting MATLAB software described previously (*38*). Positions were linked to a track if they appeared in consecutive frames within a window of 5 pixels (0.57 μm).

Bound and diffusing molecules were distinguished by calculating an apparent diffusion coefficient D_{app} from the mean square displacement (MSD) for each track, correcting for the measured localization standard deviation of ~40 nm here. Tracks with $D_{app} < 0.1$ μm^2/s were classified as bound on the basis of the bimodal shape to the distribution of D_{app} (fig. S5A). MSD traces for the diffusing molecules were calculated by averaging all tracks that were classified as unbound (SU, RR-L, Garza de Leon, F., DJS. & Kapanidis, A., unpublished), (Fig. 1F, fig. S5B) generating linear traces indicative of Brownian diffusion over our time scale of observation (0-600 ms). Our analysis suggested that up to 50% of tracks were immobile. This was higher than that predicated from slimfield by a factor of ~2. The fluorescence intensity of a single complex with a relative stoichiometry of 4:4:2 or 2:4:2 for MukB:E:F is significantly higher than our single molecule detection sensitivity for slimfield, so slimfield under-sampling of the immobile population is unlikely to account for this ~2-fold difference. This might

indicate the presence of a fast diffusing population of single molecules that were not detected at 50 ms exposure time.

Apparent diffusion coefficients of mobile MukB, E and F were at least three orders of magnitude greater than measured previously for DNA loci markers on the bacterial nucleoid (*39*) but were typically an order of magnitude lower than bacterial cytoplasmic proteins of comparable molecular weight known not to interact significantly with the nucleoid (*40*). We found that mobile MukB, E and F fluorescent spots all had very similar diffusion coefficients despite large differences in the individual molecular weights of the MukB, E and F components (MukB, 170 kDa; MukE, 26 kDa; MukF, 50.6 kDa), consistent with each tracked molecule being part of the same type of stoichiometric MukBEF complex as opposed to an individual molecular component of either MukB, E or F.

PAmCherry fluorescence over a PALM movie accumulated in 1-3 elongated spots per cell (Fig. 1F), similar to the spots identified in YPet slimfield. To analyze the spatial distribution of molecules and account for multiple consecutive localizations of each molecule, we performed clustering analysis on the mean position of bound tracks. Localizations were assigned to the same cluster if separated by less than a threshold distance. To identify the 1-3 main clusters per cell (corresponding to the diffraction-limited YPet spots), we used a threshold distance of 200 nm (5 times our measured localization precision). To identify sub-clusters of localizations within the main clusters, we used a threshold of 80 nm (2 times localization precision). With super-resolution localization, we were now able to resolve these spots into typically ~1-3, or more rarely

up to ~5, isolated sub-clusters, each containing a mean of ~10-11 immobile PAmCherry molecules for MukB and MukE, and around ~7 for MukF.

Pair-wise distances between mean localizations of molecules in sub-clusters were within our measured localization precision of ~40 nm, consistent with each sub-cluster corresponding to several closely associated MukBEF complexes (fig. S5C).

To estimate stoichiometry, we counted the number of tracks per cluster (fig. S5D). The mean values from these distributions were lower than those compared to slimfield measurements, which was expected due to the stochastic activation of fluorophore tags in PALM experiments that leaves some level of dark population implying an under-sampling of the real number of clusters present. However, since we expect the proportion of dark to photoactive flurorophore population per cell to be approximately the same for each experiment on different MukBEF components performed under the same conditions, the ratio between the mean stoichiometry values for each should be relatively unaffected. Our data indicates that the ratio from these mean values of MukE:B is 1.03 ± 0.09 (±s.e.m.), of MukE:F is 0.52 ± 0.09, and of MukB:F is 0.56 ± 0.09, consistent with the results from slimfield imaging to within experimental error.

Convolution modeling of fluorescence intensity of diffuse cytoplasmic YPet

Here, we used a similar approach to that reported previously (*9*). In brief, the mean intensity per pixel $I_m(x_0,y_0,z_0)$ of area dA at point (x_0,y_0,z_0) not within a localized fluorescent spot was modeled as the 3D convolution integral of the point spread function $P(x,y,z)$ of a single YPet molecule with the spatial distribution for the number density per unit volume V of YPet in the cell $dN/dV(x,y,z)$ and normalized local excitation intensity $L(x,y,z)$ (estimated directly from the slimfield confocal excitation field) multiplied by the intensity due to a single YPet molecule I_{YPet}:

$$I_m\left(x_0,y_0,z_0\right)dA = I_{YPet}\frac{dN}{dV}\otimes P\otimes L = I_{YPet}\iiint_{cell}\frac{dN}{dV}P(x-x_0,y-y_0,z-z_0)L(x,y,z)dxdydz$$

$$= nI_{YPet}\iiint_{cell}P(x-x_0,y-y_0,z-z_0)\exp\left(-\left(\frac{x^2}{2l_x^2}+\frac{y^2}{2l_y^2}+\frac{z^2}{2l_z^2}\right)\right)dxdydz$$

$$\equiv nI_{YPet}S$$

Here, S is the integral performed over the full extent of the cell. This generated an estimate for the total number of YPet molecules not localized in fluorescent hotspots but diffuse in the cell cytoplasm on a cell-by-cell basis, from the product of the number density n with the volume of the cell (mean value ~16,500 voxels). The function L is approximated as a 3D Gaussian with $l_x = l_y = \sigma_{xy} = 3.0$ μm and $l_z \approx 2.5\sigma_{xy} = 7.5$ μm (*9*). We estimated the mean pixel intensity not associated with localized spots for each strain after subtracting the contribution from cellular autofluorescence (~30 counts per pixel, assessed by imaging the parental non-YPet cell strain under the same microscopy conditions) and dark noise background (~1,000 counts per pixel).

The distributions of these copy number data for each cell strain were then generated using a KDE analysis similar to that used for stoichiometry estimation in localized

fluorescent spots. The KDE distributions could be fitted well using a *Random Telegraph Model* for gene expression (*41*) resulting in a Gamma probability distribution $p(x)$, similar to that reported from previous studies on the cellular copy number distribution of a variety of other bacterial proteins (*42*), such that:

$$p(x) = \frac{x^{a-1}e^{-x/b}}{b^a \Gamma(a)}$$

Here, $\Gamma(a)$ is a Gamma function. The parameters a and b are determined from the two *moments* of the Gamma distribution by its mean value m and standard deviation σ, such that $a = m^2/\sigma^2$ and $b = \sigma^2/m$. These fits were then used to determine peak values and half width at half maximum (HWHM) values (fig. S6, table S5).

Dual color single molecule millisecond fluorescence imaging and analysis

A bespoke dual color single molecule fluorescence microscope was employed by modifying the existing single color 532 nm laser excitation slimfield microscope design (Supplementary Methods). Here, we implemented two additional continuous wave TEM00 laser excitation sources for wavelengths 473 nm (B4-40, Elforlight) for GFP excitation, and 561 nm (SLIM-561, Laser2000) for mCherry excitation, each of comparable beam size to the original 532 nm single color slimfield laser, simultaneously coupling in the beams to a common laser excitation path via application of a laser line dichroic at 473 nm (Semrock) (fig. S1D). Both beams were circularized for polarization using an achromatic λ/4 plate and a dual-pass green-red dichroic mirror (61005bs, Chroma) was employed to reflect both lasers onto the sample and transmit fluorescence emissions simultaneously from GFP and mCherry fluorescent proteins from live bacterial fusion mutants. The intensity was adjusted separately for each laser using neutral density filters to match the measured mean GFP and mCherry exponential photobleach times obtained from slimfield data of dual color single-label control cell strains, i.e. in which one of the three Muk components had been labeled using either just GFP or mCherry, (Supplementary Methods) to those of the comparable cell strains in which the corresponding Muk component had been labeled only with YPet, which corresponded to typical excitation intensities of ~4.9 kW cm^{-2} and~2.9 kW cm^{-2} for the 473 nm and 561 nm laser beams respectively.

Laser bleed-through was blocked on the emission path using notch rejection filters (ZET473-NF, Chroma; NF03-561E, Semrock). A 300 mm focal length tube lens

formed an intermediate image permitting spatial filtering via a rectangular crossed-slit aperture to avoid ultimate crossover of separate different color images at the camera image plane. Following this crossed-slit aperture the beam was re-collimated via a 50 mm focal length lens and directed through a bespoke color-splitter module consisting of a dichroic mirror centered on a wavelength of 560 nm (XF2016, Omega Optical Inc.), which transmitted ~red spectral emissions and reflected ~green spectral emissions from the sample. A combination of three mirrors (fig. S1D) were then used to direct the separate green and red emissions through additional filters centered on 525 with a bandwidth of 50 nm (FF01-525/50-25, Semrock) and a 594 nm long-pass filter (BLP01-594R-25, Semrock) respectively, and a 50 mm larger diameter 150 mm focal length imaging lens which formed green and red channel images on separate halves of the same 128x128 pixel EMCCD camera detector.

The separate green and red channel images could be independently steered using mirrors in the color-splitter module, and were aligned using a control sample of a 1:500 dilution of 200 nm orange (540/60) fluorescent microspheres (F8809, Molecular Probes) incubated for 5 min in an inverted standard flow-cell (*10*), then washing away any non-stuck beads with excess minimal media buffer. This resulted in a random pattern of microspheres stuck non-specifically to the glass coverslip of the flow-cell, with a typical microsphere separation of a few microns. The spectral emissions of these orange beads bled through into both the green and red channels, allowing precise alignment of the separate images through iterative Gaussian fitting of the microsphere intensity centroids (see Supplementary Methods) which could localize the centroid of these relatively bright beams to a precision of ~10 nm, permitting the *x*-offset on the camera between the two

channels to be set to zero and the *y*-offset to be set to 64 pixels, thereby maximizing the available camera pixel array for simultaneous dual-color imaging.

In separate experiments, purified GFP and mCherry control samples were prepared using the same antibody surface-immobilization protocol as described previously (*10, 43*) utilizing anti-GFP and anti-mCherry antibodies respectively (fig. S7A). These samples were then imaged using the same microscope and laser settings as for live-cell imaging, with the resultant *in vitro* data fed through the same automated image analysis algorithms resulting in the detection of surface localized fluorescent spots which would last for typically 4-6 image frames for GFP and up to ~2 images frames for mCherry. This indicated negligible bleed-through of fluorescence of GFP into the red channel and mCherry into the green channel, as well as negligible excitation of GFP from the 561 nm laser and mCherry from the 473 nm laser, consistent with the known spectral properties of the two fluorescent proteins and with the published spectral transmission data of the dichroic mirrors and filters employed on the emission path of our dual color microscope. We set the 'on' detection threshold to be all intensities above the measured dark noise corresponding to a region of interest of the same size and shape, equivalent to a standard deviation σ of ~100 counts, and calculated the mean of all detected spot intensities above this threshold. This indicated mean single molecule brightness values of 780 ± 200 counts and 210 ± 120 counts on our camera detector for GFP and mCherry respectively, which compared with 1,100 ± 260 counts using the same protocol for YPet for the single colour slimfield imaging (fig. S7B). Although it is currently technically too challenging to isolate and purify single molecule MukBEF components tagged with either mCherry, GFP or YPet to perform an *in vitro* surface-immobilization assay as described, our

previous findings of the bacterial replisome components labeled with YPet (*9*) indicate that the presence of the tagged protein next to the fluorophore in addition to any differences in physico-chemical environment between the *in vitro* assay and the live-cell results in a difference of fluorophore brightness between the *in vitro* and *in vivo* environments of less than 10%.

To estimate the molecular stoichiometry of the Muk components in localized spots from the dual-label and single color GFP/mCherry control cell strains (see Supplementary Methods) a similar protocol was followed as for that used on the YPet cell strains except to locate the initial 'hotspots' we used the color channel which had the highest spot signal intensity with respect to background noise which, for the dual-label and GFP-only cell strains was the green channel and for the mCherry-only cell strains was the red channel. Each initial hotspot intensity centroid was then mapped onto the comparable spatial location of the alternate color channel to generate both a green channel and a red channel equivalent initial hotspot location, and then the precise intensity centroid of each hotspot was measured using separate iterative Gaussian fitting in each channel, allowing estimation of the spot intensity by the same method used for the YPet cell strains.

Intensity values in each color channel for each detected localized spot were then converted into a stoichiometry estimate using a similar method as for the YPet cell strains of estimating the initial spot intensity I_0 from a single exponential decay fit to the spot intensity values in each separate color channel, and then dividing I_0 by I_{FP}, where I_{FP} is the relevant single molecule fluorescent protein brightness for each respective channel, either ~780 counts for the green channel or ~210 counts for the red channel. The

stochiometry distribution in each channel was then rendered as an unbiased kernel density

Fluorescence Recovery after Photobleaching (FRAP)

For FRAP experiments, imaging was performed using a widefield spinning disk imaging system (PerkinElmer) and 100x objective. Images were acquired using Volocity imaging software. FRAP was performed by pulse-bleaching using a 488 nm laser for 10-15 ms and 6-15% laser intensity (radius of the spot was diffraction limited at ~300 nm). Two pre bleach images were taken, bleach spot was centered on one Muk focus and recovery of bleached region was recorded every 15 sec after bleaching, for a total time of 3 min, or for every 20 seconds after bleaching, for a total time of 5 min. Image capture was done at a 300 ms frame rate (4-6% 532 nm laser).

Quantification of FRAP intensity data

Images were analyzed using ImageJ. In brief, a background intensity was subtracted, a region of interested (ROI) was drawn around the bleached (FRAP) or unbleached (FLIP) spot and a larger ROI was drawn around the cell to measure total cellular fluorescence. Total intensity of the ROIs was measured using ImageJ. Intensity of the ROIs was normalized to the highest pre bleach intensity. These values were then corrected for photobleaching due to fluorescence excitation. The correction factor at each time point was calculated by comparing the total cellular intensity before and after each image exposure. Thus, the normalized, corrected intensity I of a ROI at time t is:

$$I(t) = (Ib(t)/Ib_{max}) /(Ic(t)/Ic_{max})$$

Where:

$Ib(t)$= intensity of ROI at time t (post bleach).

Ib_{max} = maximum intensity of ROI (pre bleach).

$Ic(t)$= intensity of whole cell at time t.

Ic_{max} = intensity of whole cell soon after bleach.

Modeling turnover of MukBEF-YPet complexes

Here, we applied a similar analytical molecular turnover model to that described previously (*9*). We modeled the experimental FRAP results of the MukBEF YPet strains (Fig. 3) as turnover of SMC dimer of dimers (MukB:E:F=4:4:2) subunits binding to and unbinding from DNA within a closed reaction-diffusion environment confined to the finite volume of the cell in which total cell content of the 4:4:2 complex is in steady-state. Here we denote:

$S_F(t)$ = Unbound number of YPet-labeled SMC dimer of dimers at time t ($t \geq 0$) following initial focused laser bleach.

$S_B(t)$ = DNA-bound number of the YPet-labeled SMC dimer of dimers in a given localized spot subjected to FRAP investigation.

$S_T(t)$ = Total number of YPet-labeled SMC dimer of dimers in the cell.

$S_B^*(t)$ = DNA-bound number of photoactive YPet-labeled SMC dimer of dimers in a given localized spot subjected to FRAP investigation.

f = Fraction of YPet-labeled SMC dimer of dimers photobleached following initial focused laser FRAP bleach.

k_1 = On-rate per YPet-labeled SMC dimer of dimers for binding to DNA in a given localized spot.

k_{-1} = Off-rate per YPet-labeled SMC dimer of dimers for unbinding from DNA in a given localized spot.

Since YPet-labeled SMC dimer of dimers is in steady-state:

$\frac{\partial S_T}{\partial t} = 0$. Thus, S_T = constant= $S_F + S_B$

We denote the full reaction-diffusion equations as:

$$\frac{\partial S_F}{\partial t} = D\nabla^2 S_F$$

$$\frac{\partial S_B}{\partial t} = k_1 S_F - k_{-1} S_B$$

D is the effective diffusion coefficient of the YPet-labeled SMC dimer of dimers not bound to the DNA. As found previously for the earlier replisome study, the typical diffusion time scale τ is set by $\sim L^2/D$ where *L* is the typical length dimension of the cell ~1 μm and *D* we estimate here from single particle tracking live-cell PALM data to be in the range ~0.1-1 $\mu m^2/s$ for the relatively mobile fluorescent spots (Supplementary Methods). This indicates a range of τ of ~0.1-1 s, which is ~2 orders of magnitude smaller than the time scale over which we observe turnover from our experimental FRAP data. Thus this is a *reaction-limited* regime, simplifying the analysis significantly. At equilibrium (for example, before the focused laser bleach) we can state that:

$$\frac{\partial S_{B,eq}}{\partial t} = 0 \therefore k_1 S_{F,eq} = k_{-1} S_{B,eq} \therefore k_1 = \frac{k_{-1} S_{B,eq}}{S_T - S_{B,eq}}$$

Where $S_{B,eq}$ and $S_{F,eq}$ are the values of S_B and S_F respectively at equilibrium. We assume the binding kinetics of photoactive SMC dimer of dimers are identical to those of photobleached SMC dimer of dimers and that the population of bleached and non-bleached are ultimately well-mixed, thus:

$$S_B^* = S_B(1-f)$$

Under general non-equilibrium conditions this indicates:

$$\frac{\partial S_B}{\partial t} = k_1 (S_T - S_B) - k_{-1} S_B$$

Solving and substituting indicates:

$$S_B^*(t) = S_B(t)(1-f) = \frac{1-f}{k_1+k_{-1}}\left(k_1 S_T - \left(k_1 S_T - \left(k_1+k_{-1}\right)S_B(0)\right)\exp\left(-\left(k_1+k_{-1}\right)t\right)\right)$$

$$= (1-f)\left(S_{B,eq} - \left(S_{B,eq} - \frac{S_B^*(0)}{1-f}\right)\exp\left(-\left(k_1+k_{-1}\right)t\right)\right)$$

$$= S_{B,eq}^*\left(1-\left(1-\frac{S_B^*(0)}{S_{B,eq}^*}\right)\exp\left(-k_{-1}t\left(1+\frac{S_{B,eq}}{S_T - S_{B,eq}}\right)\right)\right)$$

$$= S_{B,eq}^*\left(1-(1-\alpha)\exp\left(\frac{-k_{-1}S_T t}{S_T - S_{B,eq}}\right)\right)$$

Here α is the ratio of the bound photoactive component of SMC dimer of dimers at zero time (i.e. immediately after the initial focused laser bleach) to the bound photoactive component of SMC dimer of dimers at equilibrium. Since the fluorescence intensity $I_B(t)$ of the bound YPet-labeled SMC dimer of dimers component is proportional to the number of photoactive YPet-labeled SMC dimer of dimers subunits, we can write:

$$I_B(t) = I_{B,eq}\left(1-(1-\alpha)\exp\left(\frac{-k_{-1}S_T t}{S_T - S_{B,eq}}\right)\right)$$

$$= I_B(\infty)\left(1-(1-\alpha)\exp\left(\frac{-k_{-1}S_T t}{S_T - S_{B,eq}}\right)\right)$$

We estimate that a mean of ~8-10 SMC dimer of dimers subunits are present in each localized fluorescent spot, assumed to have a value of $S_{B,eq}$. Convolution modeling (Supplementary Methods) indicated ~300-400 MukB and MukE molecules and ~200 MukF molecules which are not associated with the DNA. Power spectral analysis of these more mobile spots suggests that ~30% of MukBEF complexes in the cytoplasm are in the 4:4:2 conformation (see Supplementary Methods). This indicates that the total combined

number of 4:4:2 MukBEF subunits either bound to DNA or free in the cytoplasm, $S_T(t)$, is ~30-40 complexes per cell.

The mean post bleach FRAP data were then fitted using a function $I(t)=A+B\exp(-t/t_r)$, with A and B as constants and t_r is the equivalent $1/e$ recovery time. This indicates a mean recovery time across the MukB-, MukE- and MukF-YPet datasets of 42 ± 7 s. Substituting in these values indicates k_{-1} = 0.02 ± 0.01 MukBEF 4:4:2 subunits per sec. The majority of wild type cells had two spots per cell, allowing both FRAP and FLIP analysis to be performed – these traces reached similar intensity levels to within experimental error after a few hundred seconds indicating that MukBEF complexes in the spots are in steady-state with the diffuse pool. FRAP experiments performed on wild type cells containing just one spot per cell also indicated recovery of fluorescence over a similar time scale to the 2 spot cells.

Applying the same analysis to cephalexin-elongated cells (Fig. 3, fig. S10) indicated a mean recovery time across the MukB-, MukE- and MukF-YPet datasets of 76 ± 21 s. The range of elongated cell lengths measured was 4-8 μm, suggesting a total content of MukBEF greater by a factor of at least ~2 compared to the non-elongated cells assuming similar cellular concentration levels to wild type, which was consistent with final mean recovery intensity values being ~60% for the elongated cells compared to ~30% for the non-elongated cells. Substituting these values in to the reaction-diffusion equation indicates the same estimated value of MukBEF 4:4:2 off-rate as for that estimated from the non-elongated cell FRAP data to within experimental error.

Stoichiometry analysis for rapidly diffusing 'dim' spots

The power spectra indicated in fig. S12 for the pair-wise difference distribution of the kernel density estimation of the underlying stoichiometry distribution for diffuse spots in each cell strain are generated from the square of the Fast Fourier Transform (FFT) of these data, and there is a linear dependence with square of the amplitude for detected peaks $A^2_{\text{n-mer}}$ with the number of polled periodic features to the distribution. In the case of there being potentially a mixed population of MukB:E:F complexes in either a 4:4:2 or a 2:4:2 conformation then, for the MukB component, $A^2_{\text{2-mer}}$, i.e. the square of the amplitude associated with a periodicity of ~2 molecules, is a measure of the number, N_{242}, of the 2:4:2 conformation present in the population of diffuse spots as a proportion of all MukBEF complexes, whereas $A^2_{\text{4-mer}}$ is a measure both of the sum of the 4:4:2 and 2:4:2 components, *plus* the harmonic contribution due to the ~2-mer periodicity of the 2:4:2 state being polled at ~4-mer intervals.

For features that have *precise* 2-mer periodicity then the 4-mer harmonic contribution will be polled 0.5 times as often as the fundamental 2-mer periodicity in the FFT, and so the corresponding peak on the power spectrum corresponding to $(\text{FFT})^2$ therefore will be $(0.5)^2$ or 0.25 that of the fundamental 2-mer peak. However, in practice the 2-mer periodicity is not precise across the stoichiometry distribution due primarily to noise-related dephasing, especially so at higher values of stoichiometry as a result of increased photon noise from the detected spots, and so the harmonic contribution to the 4-mer peak from the 2-mer periodicity is likely to be less than 0.25. Since the MukF component for both conformations of MukBEF complexes has only a fundamental 2-mer

periodicity, the relative size of the 4-mer peak can be used as a representative measure for the harmonic contribution from the 2-mer periodicity in this live-cell system. Put mathematically:

$$A^2_{\text{2-mer,MukB}} = \alpha N_{242}$$

$$A^2_{\text{4-mer,MukB}} = \alpha N_{442} + \beta N_{242}$$

Here, α and β are constants, with β approximated as:

$$\beta = A^2_{\text{4-mer,MukF}}/A^2_{\text{2-mer,MukF}}$$

Using this approximation, the data of fig. S11 indicate a typical value of β in the range 0.1-0.2. For each cell strain, the ratio $\rho = N_{442}/N_{242}$ can be calculated using the three equations above, such that:

$$\rho = A^2_{\text{4-mer,MukB}}/A^2_{\text{2-mer,MukB}} - A^2_{\text{4-mer,MukF}}/A^2_{\text{2-mer,MukF}}$$

The relative proportion of the number of MukBEF complexes in the two different states, $R = N_{442}:N_{242}$, is then given as $\rho/(\rho + 1):1/(\rho + 1)$. Using these analyses, the wild type and MukB_{EQ} data of fig. S12 are both consistent with $R = (0.3 \pm 0.1):(0.7 \pm 0.1)$, whereas the Muk_{DA} data indicates $(0.0 \pm 0.1):(1.0 \pm 0.1)$, in other words a ~30%:70% mix of 4:4:2 and 2:4:2 for the wild type and ATP hydrolysis mutants respectively, but principally just the 2:4:2 state for the ATP binding mutant.

Estimating the likelihood for "chance" co-localization of diffuse spots

Following a similar 2D treatment to the 3D analysis previously performed (*44*), call $p(r)dr$ the probability that the nearest neighbor to a single MukBEF complex diffuse in the cytoplasm and present in the 2D focal plane is a distance between r and $r+dr$. This must be equal to the probability that there are zero particles in range 0-r, multiplied by the probability that a single particle exists in the annulus between r and $r+dr$. Therefore:

$$p(r)dr = \left[1 - \int_0^r p(r')dr'\right] 2\pi r n dr$$

Here, n is the number of equivalent particles per unit area in the focal plane. Implying:

$$\frac{d}{dr}\left(\frac{p}{2\pi r n}\right) + 2\pi r n \cdot \frac{p}{2\pi r n} = 0$$

This indicates an integrating factor $\exp\left(\int 2\pi r n dr\right)$, therefore:

$\frac{p}{2\pi r n}\exp\left(2\pi r n dr\right) = B$, or $\frac{p}{2\pi r n}\exp\left(\pi r^2 n\right) = C$, where B and C are constants. In the limit $r \to 0$, $p \to 2\pi r n$, therefore:

$$p(r) = 2\pi r n \exp\left(-\pi r^2 n\right)$$

Thus, the probability $p_1(w)$ that the nearest neighbor particle separation is greater than a distance w is (*45*):

$$p_1(w) = 1 - \int_0^w p(r)dr = 1 - \int_0^w 2\pi r n \exp(-\pi r^2 n)dr = \exp\left(-\pi w^2 n\right)$$

The effective area density n at the focal plane is given by the number of cytoplasmic MukBEF complexes N_{focus} in the cell that are in focus divided by the cross-sectional area A of the cell which is bisected by the focal plane. N_{focus} is approximated by the number of

complexes which are included in the 'optical slice' which is bounded by the objective lens' depth of field (0.2 μm in our case). For a typical *E. coli* cell of width ~1 μm, this equates to ~1/5 of the total number N_{cyt} of cytoplasmic MukBEF complexes in the whole cell. The probability p_{chance} that a nearest neighbor MukBEF complex will be a distance less than w away is given by $1-p_1$, but if w is in effect the optical resolution limit then this equates to the probability the a 'multimer' spot is mistakenly observed by chance co-localization of two monomer MukBEF complex spots. Therefore:

$$p_{chance}=1-\exp(-\pi w^2 N_{cyt}/5A)$$

Using the MukE and MukF estimates (table S5) for N_{cyt} (since these components both have the same relative stoichiometry in either the 4:4:2 or 2:4:2 MukB:E:F complex, unlike MukB), indicates a mean of 90 ± 40 MukBEF complexes per cell diffuse in the cytoplasm. The lateral area in the focal plane for typical *E. coli* cells we estimate to be ~2,300 pixels^2, and the optical resolution limit is equivalent to ~6.6 pixels for our microscope. Substituting in these values indicates that $p_{chance} \approx 65 \pm 19\%$; this comparatively high likelihood is intuitively reasonable if one considers the effective nearest neighbor separation d_u on the more naïve assumption of a uniform spatial distribution of complexes i.e. assuming that the total cell volume estimated at typically ~16,500 pixels^3 equates to $4\pi N_{cyt}/3(d_u/2)^3$, suggesting d_u ~7 pixels or ~280 nm, only ~20% larger than the optical resolution limit – though taking into account a potential ~20% volume exclusion by the bulk of the nucleoid suggests a revised estimate for d_u of ~260 nm, only ~10% larger than the optical resolution limit.

The stoichiometry distribution data of fig. S12, for the MukE and MukF components, indicates that the probability for observing a multimer (i.e. MukE

component ~8 or more, MuF components ~4 or more) is in excess of ~80%. In other words, this is consistent with most of the apparent ‘multiple’ MukBEF spots diffuse in the cytoplasm being most likely chance co-localization events of two or more single MukBEF complexes separated by less than the optical resolution limit and so observed as a single spot, but there was still a minority of multiple events that are due to ‘real’ multimers (most likely dimers) in the MukBEF cytoplasmic pool.

The dimer pairs undergo independent hydrolysis to release an SMC dimer of dimers complex from DNA

Previous *in vitro* measurements of the ATPase activity of MukB ATPase heads in the presence of MukEF indicate a range of 5.6-20 ATP per MukB dimer per min (*8, 19*), which is equivalent to a probability of *p* in the range 0.09-0.33 ATP per dimer per sec.

If each dimer in the two closed heads of the SMC dimer of dimers *in vivo* are required to be hydrolyzed independently for release from the DNA to occur then the turnover rate, or the probability *P* for this occurring per second, is $\sim p^2$, suggesting a range of *P* of 0.01-0.11 dimer of dimers per sec, consistent with the experimental estimates of the measured FRAP turnover rate.

Conversely, consider a different scenario in which a single SMC dimer could hypothetically be released from DNA by a coupled hydrolysis of just two bound ATPs. The dimer turnover rate is then simply $\sim p$, roughly an order of magnitude greater than the observed FRAP turnover rate.

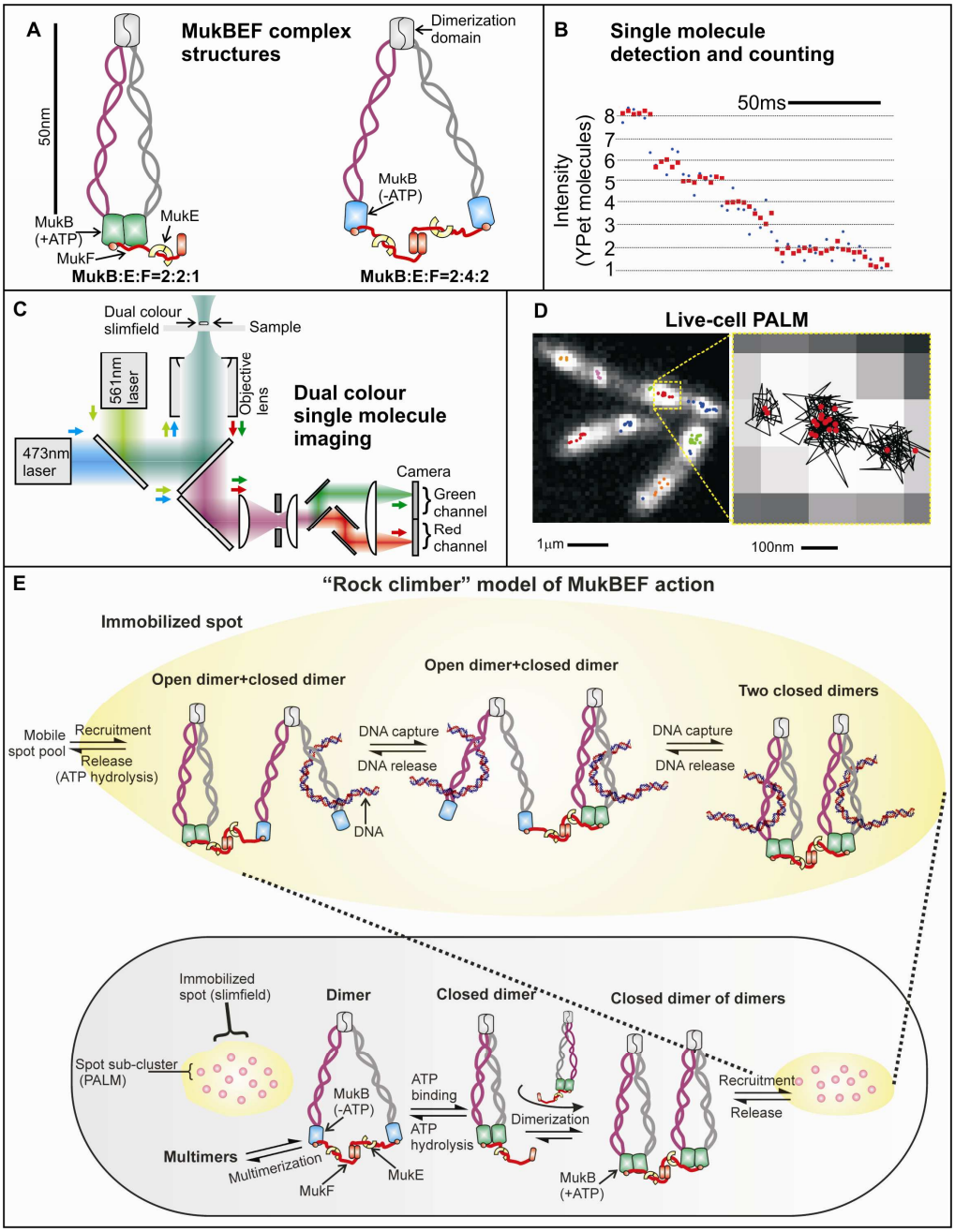

Fig. S1. Summary. **(A)** Schematic of MukBEF with ATP bound to engaged heads (green) and 1 molecule of MukF and 2 of MukE associated with each MukB dimer. Dimerization of these through the N-terminal dimerization domain of MukF *(8, 13)* can lead to the

observed dimer of dimer complexes. In the absence of ATP (cyan heads), the heads are unengaged and two molecules of MukF and 4 of MukE can associate with each dimer. *(8).* **(B)** Detection of single-molecule photobleaching events, **(C)** Dual color single-molecule ms imaging set-up. **(D)** Results from live-cell PALM to estimate molecular stiochiometry, architecture and dynamics of immobile functional complexes. **(E)** "Rock climber" model for the in vivo action of SMC complexes. Top panel: dimer of dimer 4:4:2 MukB:E:F complexes are recruited to immobile spots in the region of replication origins, where they associate with DNA. One segment of captured DNA can be released by coupled hydrolysis of the two ATPs bound to engaged dimer heads, as in related ABC transporters (*46*). Nevertheless, complete release of a dimer of dimers from DNA requires two almost simultaneous hydrolysis events in each pair of engaged heads. Consistent with this is relatively long dwell time of individual complexes (~50 s) as compared to that expected if release from DNA resulted from a single pair of concerted hydrolysis events in a dimer, as judged by *in vitro* MukBEF ATPase activity *(8, 19)* (Supplementary Methods). The release of one segment of DNA, and capture of a new segment without releasing the complex from the chromosome is proposed to underlie the molecular action of MukBEF in chromosome organization and segregation. Bottom panel. The predominant state for rapidly diffusing spots is 2:4:2, with a minority of dimer of dimer complexes, whose presence requires ATP binding. Complexes unable to bind ATP form only dimer complexes.

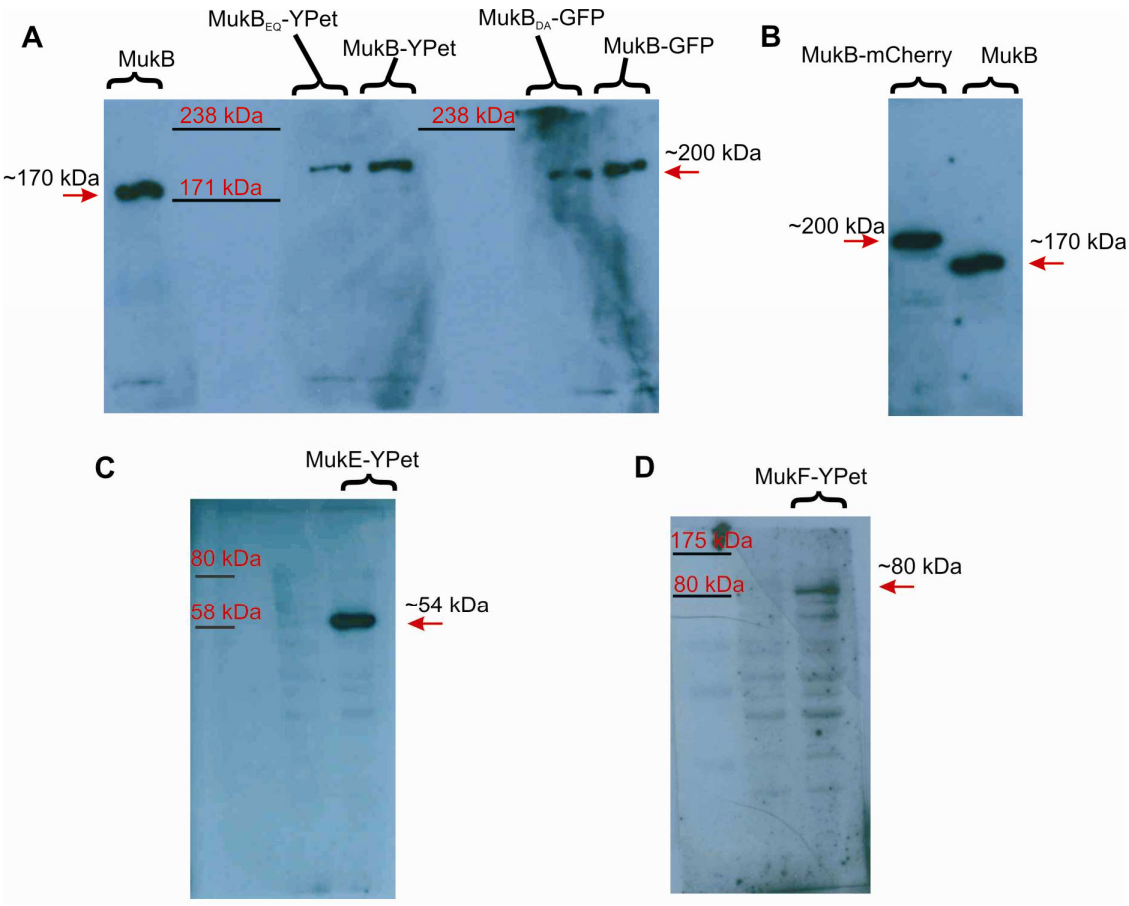

Fig. S2. Characterization of MukBEF cell strains using western blotting. Example western blots from cell strains **(A)** MukB-YPet and MukB-GFP, **(B)** MukB (non-fluorescent parental strain) and MukB-mCherry **(C)** MukE-YPet, **(D)** MukF-YPet, probed using an anti-MukBEF antibody as described in Supplementary Methods. The positions of molecular weight marker lines are indicated in kDa, as are the calculated molecular weights of the probed Muk proteins on the basis of their known sequences (red arrows).

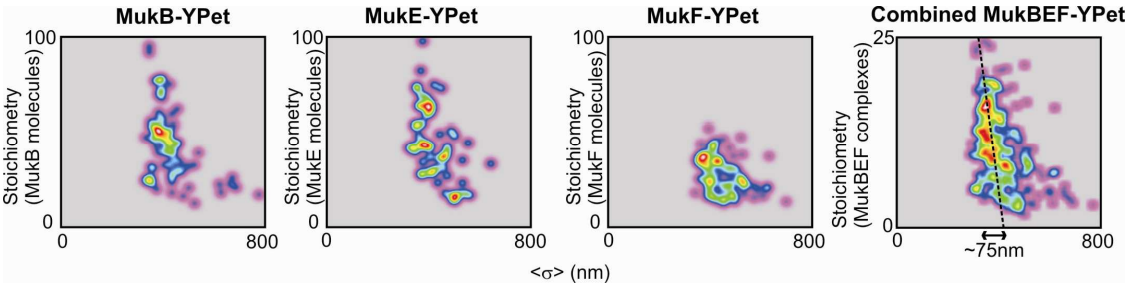

Fig. S3. Variation of spot width with stoichiometry for YPet strains. 2D false-color contour images generated using kernel density estimation via a 2D Gaussian convolution of the data for mean measured Gaussian standard deviation spot width <σ> with estimated spot stoichiometry for the three wild type Muk strains (first three panels from the left). These data are then combined using a 4:4:2 conformation model for a single MukB:E:F complex (panel far right), with a linear fit (dotted line) indicating a mean decrease of ~75 nm in spot width over a range of increase of ~25 MukBEF 4:4:2 complexes to spot stoichiometry, or ~3 nm per complex on average.

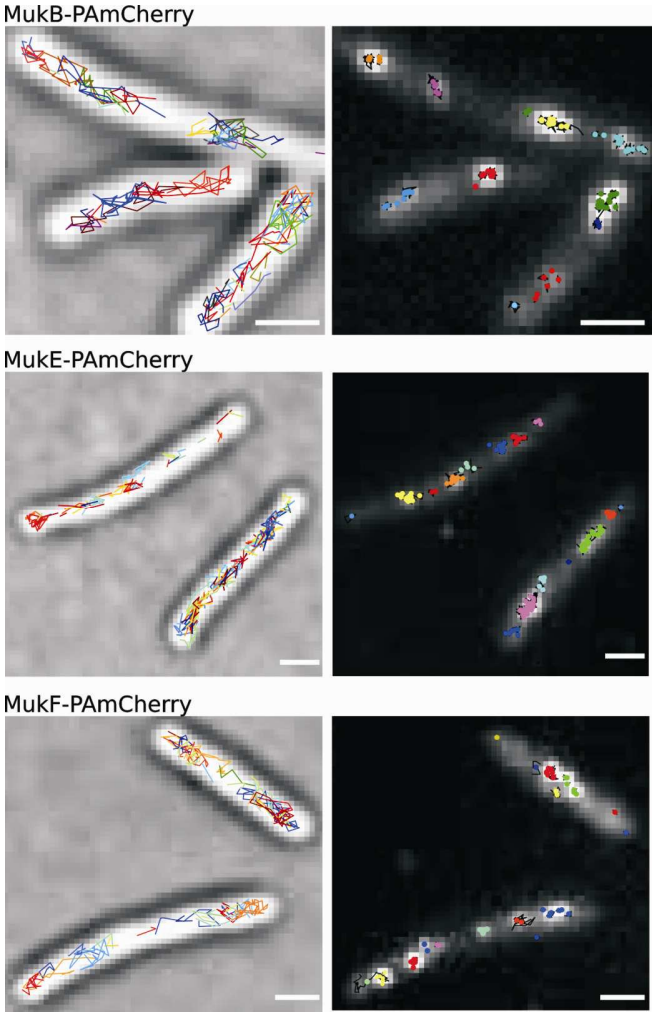

Fig. S4. PALM single particle tracking. Diffusing (left panel, colored tracks with gray brightfield overlaid) and immobile PAmCherry molecules (right panel, bound tracks and colored clustered localizations, overlaid against accumulated PAmCherry fluorescence), white bar 1 μm.

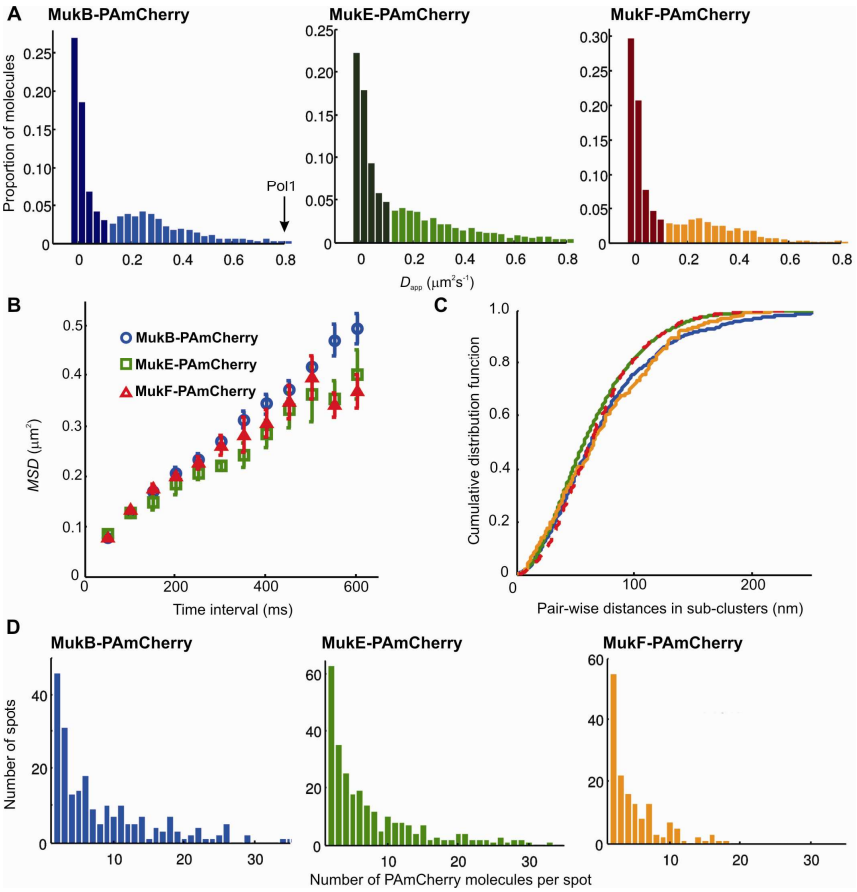

Fig. S5. Live-cell PALM. **(A)** Diffusion coefficients, Dapp for MukB-PAmCherry (blue), MukE-PAmCherry (green), MukF-PAmCherry (orange) molecules (lighter coloring putative diffusing molecules, darker colors immobile molecules). Modal value for DNA polymerase I (Pol1) measured using same technique indicated (arrow) for comparison. **(B)** Average mean square displacement for all diffusing molecules. **(C)** Cumulative distribution function of measured (same color code as for **A**) and simulated pair-wise distances between PAmCherry localizations within sub-clusters (red dashed line). Simulation based on random distribution model of localizations for a two-dimensional Gaussian distribution with width of our localization precision of 40 nm. **(D)** Distribution of MukBEF stoichiometry per elongated spot.

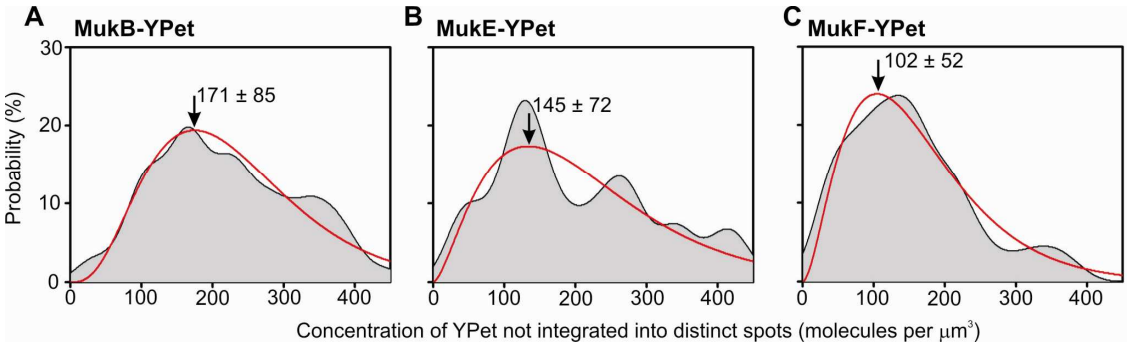

Fig. S6. Distributions of estimated concentration of YPet per cell not integrated into distinct fluorescent spots. Kernel density estimations (gray) based on convolution modeling on YPet intensity not integrated in localized spots for **(A)** MukB, **(B)** MukE and **(C)** MukF, Gamma fits indicated (red), with peak value ± half width at half maximum (HWHM) of Gamma fit.

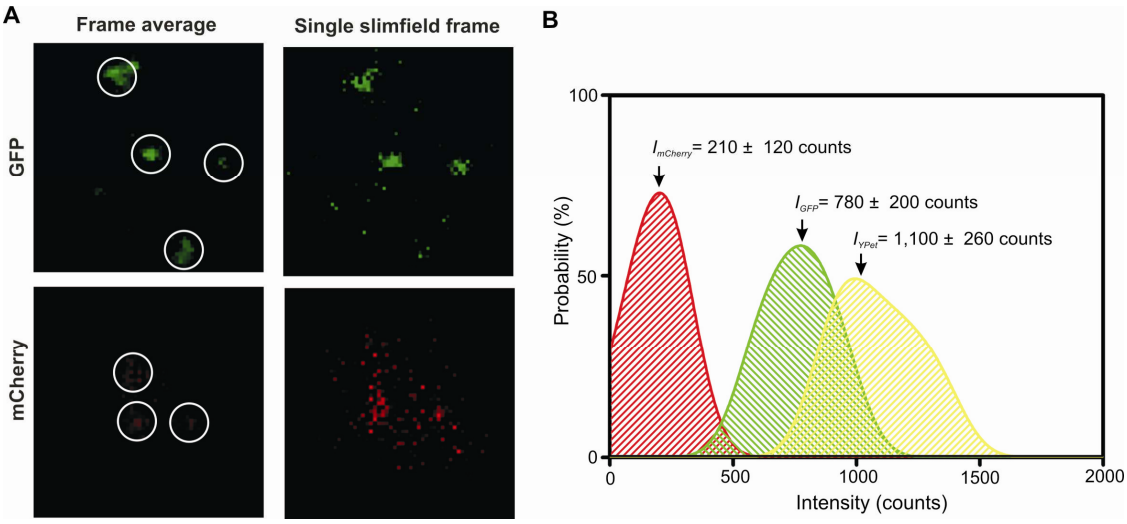

Fig. S7. *In vitro* calibration using purified GFP and mCherry. Surface immobilized GFP (green channel shown, upper panel) and mCherry (red channel shown, lower panel) with frame average image using 10 consecutive image frames (left panel) with identified single molecule hotspots (white circles), compared against single slimfield image frames (right panel). **(B)** Distribution of *in vitro* spot brightness values for mCherry (red) and GFP (green), compared against YPet (yellow), generated using 1-dimensional unbiased kernel density estimation of spot brightness values with a kernel width of 100 counts, mean and s.d values indicated (arrows), *N*=69-128 spots.

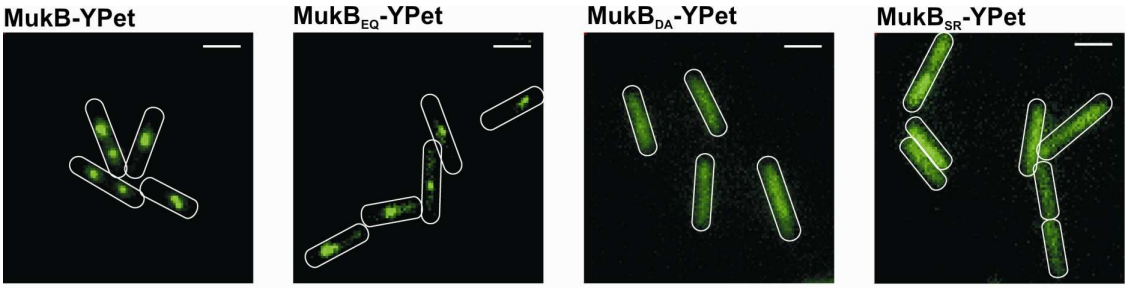

Fig. S8. The formation of localized MukBEF structures. The localized fluorescent spot phenotype of wild type (far left panel) and the ATP hydrolysis mutant $MukB_{EQ}$ compared against the ATP-binding mutants $MukB_{DA}$ and $MukB_{SR}$, shown here in variants for which the MukB component is fused to YPet (epifluorescence images, green), borders of cell indicated (white) and white scale bar indicating 1 μm.

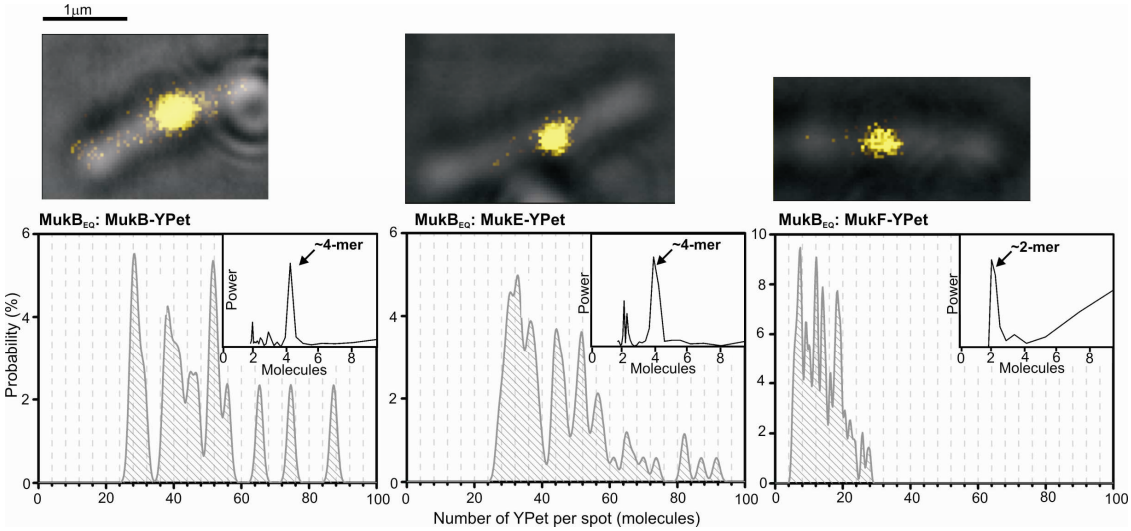

Fig. S9. Stoichiometry distributions of $MukB_{EQ}$-YPet strain spots. Brightfield (gray) and slimfield (yellow) images overlaid (upper panel) with associated stoichiometry kernel density estimation distributions, power spectra indicated (inset), *N*=55-75 traces.

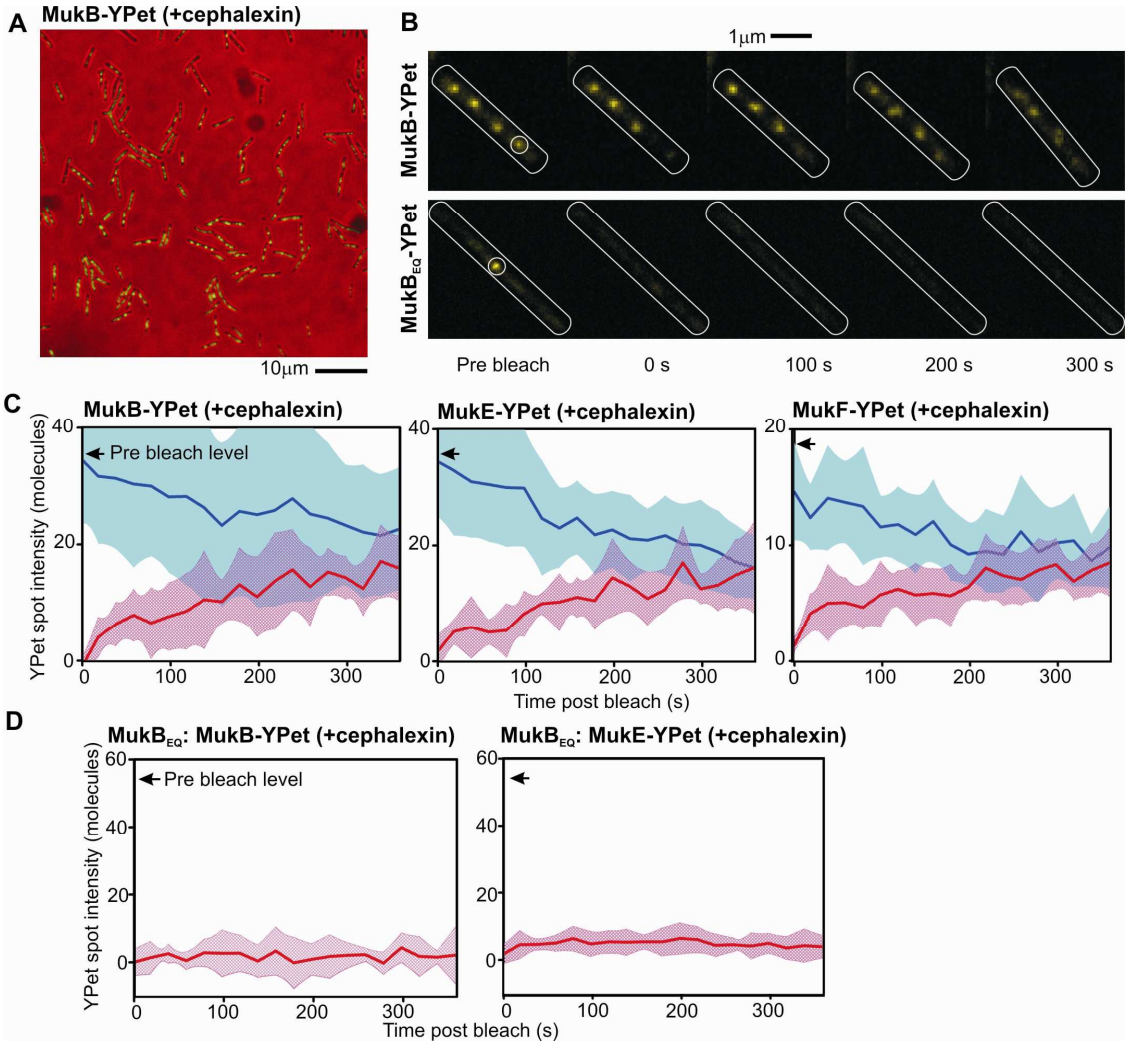

Fig. S10. Assessing molecular turnover of MukBEF components using FRAP-FLIP. (**A)** Overlaid brightfield and epifluorescence (green) images for elongated MukB-YPet cells. **(B)** Example FRAP recovery time series images on steady-state cephalexin-elongated cells for MukB-YPet wild type (upper panel) and the ATP hydrolysis mutant MukB$_{EQ}$-YPet (lower panel), cell outlines indicated (white) and approximate extent of focused laser bleach (circle). (**C,D)** Mean FRAP (red) and FLIP (blue) traces taken from steady-state cells not treated with cephalexin, for **(C)** wild type strains and **(D),** mean FRAP-only traces for the ATP hydrolysis mutants MukB$_{EQ}$-YPet and MukB$_{EQ}$:MukE-YPet.

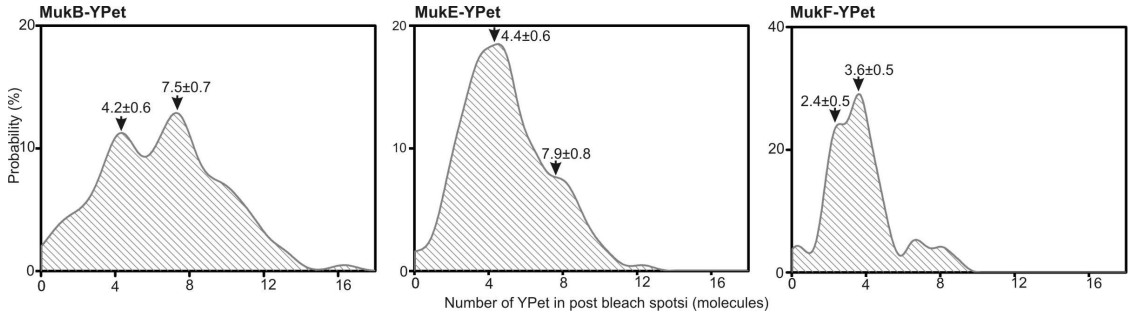

Fig. S11. Post FRAP bleach stoichiometry. Distributions of spot stoichiometry for the post FRAP bleach time points from the MukB-, MukE- and MukF-YPet cells using one-dimensional kernel density estimation. Two-Gaussian fits performed to principle peaks, with mean ± s.d. widths indicated (arrows).

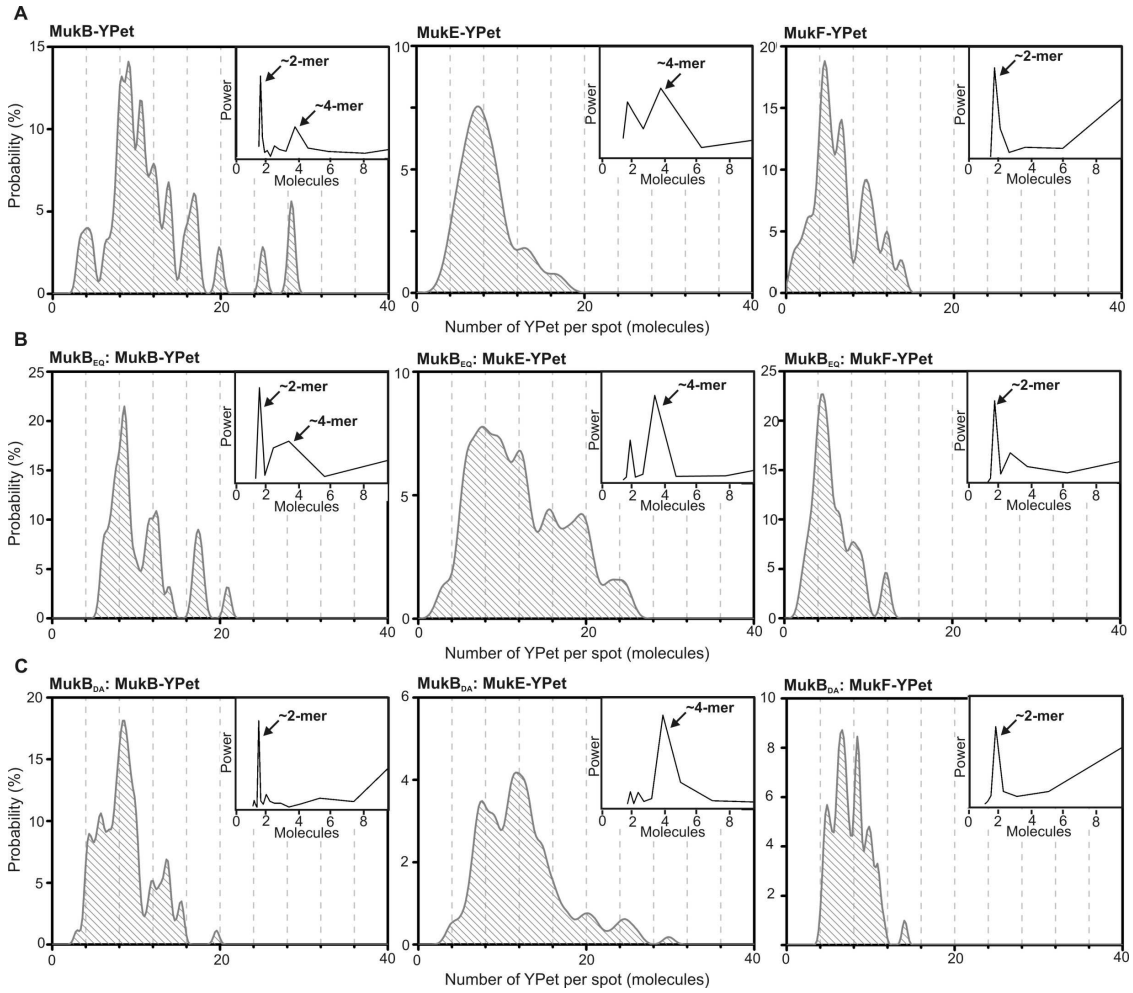

Fig. S12. Stoichiometry distributions for mobile 'diffuse' spots. Stoichiometry kernel density estimation distributions, power spectra indicated (inset), for 'diffuse' spots (i.e. spots not detected as being in a 'hotspot' region on the frame-average images) for **(A)** wild type MukBEF, (**B)** the $MukB_{EQ}EF$ mutant which can bind but not hydrolyze ATP and **(C)** the $MukB_{DA}EF$ mutant which cannot bind ATP. Grid-lines as 4-mer intervals, *N* = 35-129 traces. See Supplementary Methods.

Sample	Primary antibody	Secondary antibody
MukB-mYpet	MukB (*30*)	Anti-rabbit
MukB-mCherry	MukB (*30*)	Anti-rabbit
$MukB_{EQ}$-GFP	MukB (*30*)	Anti-rabbit
$MukB_{DA}$-GFP	MukB (*30*)	Anti-rabbit
MukE-mYPet	Anti-GFP	Anti-rabbit
MukF-mYPet	Anti-GFP	Anti-rabbit

Table S1. List of primary and secondary antibodies used for western probes.

Ab16	*mukB-YPet, Km^R*	This study
Ab18	*mukE-YPet Km^R*	This study
Ab25	*mukB-mCherry frt, mukE-YPet, Km^R*	This study
Ab24	*mukB-mCherry, Km^R*	This study
Ab36	*mukE-YPet frt*	This study
Ab45	*mukB-GFP, Cm^R*	This study
Ab60	*frt YPet-mukF*	This study
Ab75	*mukB-E1407Q-GFP, Cm^R*	This study
Ab81	*Ab60, mukBmCherry , , Cm^R*	This study
Ab88	*mukE-mCherry frt*	This study
Ab137	*Ab88, Ab75*	This study
Ab191	*frt N-mCherry-mukF*	This study
Ab198	*mukB-E1407Q-YPet, Km^R*	This study
Ab213	*mukB-E1407Q, Km^R , Ab60*	This study
Ab220	*mukB-GFP, Cm^R, Ab88*	This study
Ab221	*mukB-GFP , Cm^R, Ab191*	This study
Ab223	*mukB-E1407Q, Km^R, MukE-YPet frt*	This study
Ab237	*mukE-PAmCherry, Km^R*	This study
Ab238	*mukB-PAmCherry, Km^R*	This study
Ab246	*mukB-D1406A-mYPet, Km^R*	This study
Ab247	*mukB-D1406A Km^R , MukF-YPet frt*	This study
Ab248	*mukB-D1406A, Km^R , MukE-YPet frt*	This study
RRL80	*mukB-D1406A-GFP, Cm^R*	This study
Kat1	*mukB-GFP, Cm^R*	Ref. (*31*)

Table S2. List of strains and their sources used in current study.

Strain name	Doubling time (min) in LB, 37°C, ±s.d.	Doubling time (min) in M9-glycerol, 37°C, ±s.d.	Anucleate cells (% proportion of total population)	Cell filamentation (% proportion of total population)
AB1157 (wild type)	33±3	110±10	<1%	<1%
MukB-YPet	34±2	108±10	<1%	<2%
MukE-YPet	34±2	110±12	<1%	<2%
MukF-YPet	36±3	112±10	<1%	<2%
MukE-Cherry MukB-GFP	33±4	114±12	<1%	<2%
MukF-mCherry MukB-GFP	34±2	116±11	<1%	<2%

Table S3. Characterization of strains used in current study.

Strain	Mean number of molecules per spot averaged across all cells ±SEM	Mean number of molecules per spot: 1 spot cells (±SEM), % proportion of cells with localized spots	Mean number of molecules per spot: 2 spot cells (spot #1) ±SEM, % proportion of cells with localized spots	Mean number of molecules per spot: 2 spot cells (spot #2) ±SEM, % proportion of cells with localized spots	Mean number of molecules per spot: 3 spot cells (spot #1) ±SEM, % proportion of cells with localized spots	Mean number of molecules per spot: 3 spot cells (spot #2) ±SEM, % proportion of cells with localized spots	Mean number of molecules per spot: 3 spot cells (spot #3) ±SEM, % proportion of cells with localized spots
MukB-YPet	36±3	51.8±13.0, 9.6%	52.4±6.9, 60.4%	26.4±1.6, 60.4%	40.1±2.5, 30.0%	28.9±2.1, 30.0%	20.9±1.8, 30.0%
MukE-YPet	36±4	53.8±8.3 18.1%	53.4±3.3 61.0%	27.4±2.4 61.0%	42.2±4.2, 21.9%	26.1±3.0, 21.9%	12.0±1.6, 21.9%
MukF-YPet	19±1	28.3±3.3 17.1%	31.0±4.1 69.5%	15.0±1.5 69.5%	30.0±1.2, 13.4%	18.9±1.1, 13.4%	12.8±1.2, 13.4%
$MukB_{EQ}$-YPet	55±4	64.8±5.2, 81.8%	52.3±2.6, 18.2%	11.4±3.4, 18.2%	-	-	-
$MukB_{EQ}$: MukE-YPet	54±4	65.2±4.2, 80.0%	55.6±3.9, 20.0%	9.5±1.0, 20.0%	-	-	-
$MukB_{EQ}$: MukF-YPet	20±4	22.0±3.2, 73.1%	21.6±5.2, 26.9%	6.8±1.0, 26.9%	-	-	-

Table S4. Analysis of YPet fusion cell strains for spot stoichiometry, classed into cells of different numbers of distinct spots (ranked such that #1 is the spot with the highest measured stoichiometry for multi spot cells, in that given cell).

Strain	**Mean total number of molecules in all localized spots per cell ±SEM, *N*=number of cells in dataset**	**Total number of molecules not in localized spot per cell (Mode from Gamma fit ± HWHM)**	**Proportion of molecules in localized spots relative to number in whole cell (%)**	**Total number of molecules per cell**
MukB	82±7, *N*=96	356±177	19±10	438±180
MukE	79±3, *N* =82	301±150	21±11	380±154
MukF	45±2s, *N* =105	211±109	18±10	256±110
$MukB_{EQ}$	65±6, *N* =55	278±139	20±9	333±139
$MukB_{EQ}$MukE	65±5, *N* =75	331±166	16±8	396±166
$MukB_{EQ}$MukF	24±4, *N* =64	170±85	11±5	214±88

Table S5. Distribution of total numbers of MukBEF molecules in YPet in both the fluorescent spots and not integrated into localized spots.

Strain	Spot stoichiometry (mean±s.d.)		Number of spots in dataset
	Green channel	Red Channel	
MukB-GFP	31±14	-	41
MukE-mCherry	-	41±14	28
MukF-mCherry	-	23±10	22
MukB-GFP: MukE-mCherry	33±16	30±15	136
MukB-GFP: MukF-mCherry	29±18	14±7	115

Table S6 Localized fluorescent spot stoichiometry estimates for dual color cell strains and single color GFP and mCherry control cell strain.

References

1. S. Gruber, MukBEF on the march: Taking over chromosome organization in bacteria? *Mol. Microbiol.* **81**, 855 (2011). doi:10.1111/j.1365-2958.2011.07764.x Medline

2. K. Nasmyth, C. H. Haering, The structure and function of SMC and kleisin complexes. *Annu. Rev. Biochem.* **74**, 595 (2005). doi:10.1146/annurev.biochem.74.082803.133219 Medline

3. A. J. Wood, A. F. Severson, B. J. Meyer, Condensin and cohesin complexity: The expanding repertoire of functions. *Nat. Rev. Genet.* **11**, 391 (2010). doi:10.1038/nrg2794 Medline

4. H. Niki *et al*., *E. coli* MukB protein involved in chromosome partition forms a homodimer with a rod-and-hinge structure having DNA binding and ATP/GTP binding activities. *EMBO J.* **11**, 5101 (1992). Medline

5. K. Yamanaka, T. Ogura, H. Niki, S. Hiraga, Identification of two new genes, mukE and mukF, involved in chromosome partitioning in *Escherichia coli*. *Mol. Gen. Genet.* **250**, 241 (1996). doi:10.1007/BF02174381 Medline

6. O. Danilova, R. Reyes-Lamothe, M. Pinskaya, D. Sherratt, C. Possoz, MukB colocalizes with the *oriC* region and is required for organization of the two *Escherichia coli* chromosome arms into separate cell halves. *Mol. Microbiol.* **65**, 1485 (2007). doi:10.1111/j.1365-2958.2007.05881.x Medline

7. S. Hiraga *et al*., Mutants defective in chromosome partitioning in *E. coli*. *Res. Microbiol.* **142**, 189 (1991). doi:10.1016/0923-2508(91)90029-A Medline

8. J. S. Woo *et al*., Structural studies of a bacterial condensin complex reveal ATP-dependent disruption of intersubunit interactions. *Cell* **136**, 85 (2009). doi:10.1016/j.cell.2008.10.050 Medline

9. R. Reyes-Lamothe, D. J. Sherratt, M. C. Leake, Stoichiometry and architecture of active DNA replication machinery in *Escherichia coli*. *Science* **328**, 498 (2010). doi:10.1126/science.1185757 Medline

10. M. C. Leake *et al*., Stoichiometry and turnover in single, functioning membrane protein complexes. *Nature* **443**, 355 (2006). doi:10.1038/nature05135 Medline

11. B. Huang, M. Bates, X. Zhuang, Super-resolution fluorescence microscopy. *Annu. Rev. Biochem.* **78**, 993 (2009). doi:10.1146/annurev.biochem.77.061906.092014 Medline

12. Z. M. Petrushenko, C. H. Lai, V. V. Rybenkov, Antagonistic interactions of kleisins and DNA with bacterial Condensin MukB. *J. Biol. Chem.* **281**, 34208 (2006). doi:10.1074/jbc.M606723200 Medline

13. R. Fennell-Fezzie, S. D. Gradia, D. Akey, J. M. Berger, The MukF subunit of *Escherichia coli* condensin: Architecture and functional relationship to kleisins. *EMBO J.* **24**, 1921 (2005). doi:10.1038/sj.emboj.7600680 Medline

14. M. Gloyd, R. Ghirlando, A. Guarné, The role of MukE in assembling a functional MukBEF complex. *J. Mol. Biol.* **412**, 578 (2011). doi:10.1016/j.jmb.2011.08.009 Medline

15. M. Hirano, T. Hirano, Positive and negative regulation of SMC-DNA interactions by ATP and accessory proteins. *EMBO J.* **23**, 2664 (2004). doi:10.1038/sj.emboj.7600264 Medline

16. B. Hu *et al*., ATP hydrolysis is required for relocating cohesin from sites occupied by its Scc2/4 loading complex. *Curr. Biol.* **21**, 12 (2011). doi:10.1016/j.cub.2010.12.004 Medline

17. P. Arumugam *et al*., ATP hydrolysis is required for cohesin's association with chromosomes. *Curr. Biol.* **13**, 1941 (2003). doi:10.1016/j.cub.2003.10.036 Medline

18. S. Weitzer, C. Lehane, F. Uhlmann, A model for ATP hydrolysis-dependent binding of cohesin to DNA. *Curr. Biol.* **13**, 1930 (2003). doi:10.1016/j.cub.2003.10.030 Medline

19. N. Chen *et al*., ATP-induced shrinkage of DNA with MukB protein and the MukBEF complex of *Escherichia coli*. *J. Bacteriol.* **190**, 3731 (2008). doi:10.1128/JB.01863-07 Medline

20. C. Kural *et al*., Kinesin and dynein move a peroxisome in vivo: A tug-of-war or coordinated movement? *Science* **308**, 1469 (2005). doi:10.1126/science.1108408 Medline

21. J. Mascarenhas *et al*., Dynamic assembly, localization and proteolysis of the *Bacillus subtilis* SMC complex. *BMC Cell Biol.* **6**, 28 (2005). doi:10.1186/1471-2121-6-28 Medline

22. C. D'Ambrosio, G. Kelly, K. Shirahige, F. Uhlmann, Condensin-dependent rDNA decatenation introduces a temporal pattern to chromosome segregation. *Curr. Biol.* **18**, 1084 (2008). doi:10.1016/j.cub.2008.06.058 Medline

23. M. T. Ocampo-Hafalla, F. Uhlmann, Cohesin loading and sliding. *J. Cell Sci.* **124**, 685 (2011). doi:10.1242/jcs.073866 Medline

24. D. Gerlich, T. Hirota, B. Koch, J. M. Peters, J. Ellenberg, Condensin I stabilizes chromosomes mechanically through a dynamic interaction in live cells. *Curr. Biol.* **16**, 333 (2006). doi:10.1016/j.cub.2005.12.040 Medline

25. R. A. Oliveira, S. Heidmann, C. E. Sunkel, Condensin I binds chromatin early in prophase and displays a highly dynamic association with *Drosophila* mitotic chromosomes. *Chromosoma* **116**, 259 (2007). doi:10.1007/s00412-007-0097-5 Medline

26. C. H. Haering, A. M. Farcas, P. Arumugam, J. Metson, K. Nasmyth, The cohesin ring concatenates sister DNA molecules. *Nature* **454**, 297 (2008). doi:10.1038/nature07098 Medline

27. B. J. Bachmann, Pedigrees of some mutant strains of *Escherichia coli* K-12. *Bacteriol. Rev.* **36**, 525 (1972). Medline

28. K. A. Datsenko, B. L. Wanner, One-step inactivation of chromosomal genes in *Escherichia coli* K-12 using PCR products. *Proc. Natl. Acad. Sci. U.S.A.* **97**, 6640 (2000). doi:10.1073/pnas.120163297 Medline

29. R. Reyes-Lamothe, C. Possoz, O. Danilova, D. J. Sherratt, Independent positioning and action of *Escherichia coli* replisomes in live cells. *Cell* **133**, 90 (2008). doi:10.1016/j.cell.2008.01.044 Medline

30. M. Yamazoe *et al*., Complex formation of MukB, MukE and MukF proteins involved in chromosome partitioning in *Escherichia coli*. *EMBO J.* **18**, 5873 (1999). doi:10.1093/emboj/18.21.5873 Medline

31. K. Ohsumi, M. Yamazoe, S. Hiraga, Different localization of SeqA-bound nascent DNA clusters and MukF-MukE-MukB complex in *Escherichia coli* cells. *Mol. Microbiol.* **40**, 835 (2001). doi:10.1046/j.1365-2958.2001.02447.x Medline

32. E. Betzig *et al*., Imaging intracellular fluorescent proteins at nanometer resolution. *Science* **313**, 1642 (2006). doi:10.1126/science.1127344 Medline

33. F. V. Subach *et al*., Photoactivatable mCherry for high-resolution two-color fluorescence microscopy. *Nat. Methods* **6**, 153 (2009). doi:10.1038/nmeth.1298 Medline

34. S. Manley *et al*., High-density mapping of single-molecule trajectories with photoactivated localization microscopy. *Nat. Methods* **5**, 155 (2008). doi:10.1038/nmeth.1176 Medline

35. B. P. English *et al*., Single-molecule investigations of the stringent response machinery in living bacterial cells. *Proc. Natl. Acad. Sci. U.S.A.* **108**, E365 (2011). doi:10.1073/pnas.1102255108 Medline

36. R. E. Thompson, D. R. Larson, W. W. Webb, Precise nanometer localization analysis for individual fluorescent probes. *Biophys. J.* **82**, 2775 (2002). doi:10.1016/S0006-3495(02)75618-X Medline

37. S. J. Holden *et al*., Defining the limits of single-molecule FRET resolution in TIRF microscopy. *Biophys. J.* **99**, 3102 (2010). doi:10.1016/j.bpj.2010.09.005 Medline

38. J. C. Crocker, D. G. Grier, Methods of digital video microscopy for colloidal studies. *J. Colloid Interface Sci.* **179**, 298 (1996). doi:10.1006/jcis.1996.0217

39. C. L. Woldringh, in *Bacterial Chromatin*, R. T. Dame, C. J. Dorman, Eds. (Springer Biomedical/Life Science, Netherlands, 2009), pp. 71–96.

40. N. J. Delalez *et al*., Signal-dependent turnover of the bacterial flagellar switch protein FliM. *Proc. Natl. Acad. Sci. U.S.A.* **107**, 11347 (2010). doi:10.1073/pnas.1000284107 Medline

41. J. Peccoud, B. Ycart, Markovian modelling of gene-product synthesis. *Theor. Popul. Biol.* **48**, 222 (1995). doi:10.1006/tpbi.1995.1027

42. L. Cai, N. Friedman, X. S. Xie, Stochastic protein expression in individual cells at the single molecule level. *Nature* **440**, 358 (2006). doi:10.1038/nature04599 Medline

43. M. Plank, G. H. Wadhams, M. C. Leake, Millisecond timescale slimfield imaging and automated quantification of single fluorescent protein molecules for use in probing complex biological processes. *Integr. Biol.* **1**, 602 (2009). doi:10.1039/b907837a Medline

44. S. Chandrasekhar, Stochastic problems in physics and astronomy. *Rev. Mod. Phys.* **15**, 1 (1943). doi:10.1103/RevModPhys.15.1

45. G. J. Schütz, M. Sonnleitner, H. Schindler, Ultrasensitive microscopy of the plasma membrane of living cells. *J. Fluoresc.* **11**, 177 (2001). doi:10.1023/A:1012245016672

46. J. E. Moody, L. Millen, D. Binns, J. F. Hunt, P. J. Thomas, Cooperative, ATP-dependent association of the nucleotide binding cassettes during the catalytic cycle of ATP-binding cassette transporters. *J. Biol. Chem.* **277**, 21111 (2002). doi:10.1074/jbc.C200228200 Medline